J|A|C|S ARTICLES

Published on Web 02/26/2010

# Fe L-Edge X-ray Absorption Spectroscopy Determination of Differential Orbital Covalency of Siderophore Model Compounds: Electronic Structure Contributions to High Stability Constants

Rosalie K. Hocking,[†,‡] Serena DeBeer George,[§,⊥] Kenneth N. Raymond,[*,#] Keith O. Hodgson,[*,†,§] Britt Hedman,[*,§] and Edward I. Solomon[*,†,§]

*Department of Chemistry, Stanford University, Stanford, California 94305, Monash Centre for Synchrotron Science and School of Chemistry, Monash University, 3800 Victoria, Australia, Stanford Synchrotron Radiation Lightsource, SLAC, Stanford University, Stanford, California 94309, and Department of Chemistry, The University of California, Berkeley, California 94720*

Received October 22, 2009; E-mail: edward.solomon@stanford.edu

***Abstract:*** Most bacteria and fungi produce low-molecular-weight iron chelators called siderophores. Although different siderophore structures have been characterized, the iron-binding moieties often contain catecholate or hydroxamate groups. Siderophores function because of their extraordinarily high stability constants ($K_{STAB} = 10^{30}-10^{49}$) and selectivity for Fe(III), yet the origin of these high stability constants has been difficult to quantify experimentally. Herein, we utilize Fe L-edge X-ray absorption spectroscopy to determine the differential orbital covalency (i.e., the differences in the mixing of the metal d-orbitals with ligand valence orbitals) of a series of siderophore model compounds. The results enable evaluation of the electronic structure contributions to their high stability constants in terms of $\sigma$- and $\pi$-donor covalent bonding, ionic bonding, and solvent effects. The results indicate substantial differences in the covalent contributions to stability constants of hydroxamate and catecholate complexes and show that increased $\sigma$ as well as $\pi$ bonding contributes to the high stability constants of catecholate complexes.

## 1. Introduction

Siderophores are low-molecular-weight compounds synthesized by bacteria and fungi to facilitate the uptake of Fe(III),[1−3] the concentration of which is severely limited by the extremely low solubility of Fe(III) hydroxide and by iron-binding proteins *in vivo*. Bacterial siderophores occur in three broad groups based on the chemical nature of the chelating ligands: catecholates (e.g., enterobactin[4]), hydroxypyridonates/hydroxamates (e.g., cepabactin[5]/desferrioxamine E[6]), and aminocarboxylates (e.g., rizoferrin[7]), all of which act as strong, usually hexadentate chelating agents for Fe(III). Because of the importance of biological Fe uptake, significant effort has been directed toward making more efficient ferric chelating agents. Raymond et al.[8−10] have made a number of multidentate ligands that incorporate the catecholate and hydroxamate functionalities to mimic the biological sequestering of Fe(III), and these have been used in a number of medical (e.g., oral iron chelation treatment[11,12]) and industrial (e.g., radionuclide separation[13,14]) applications. Understanding the factors leading to the high stability and Fe(III) selectivity of the siderophores has important implications in controlling Fe transport in biology and may lead to the design of more effective chelating agents.

The high binding constants have enthalpic (covalent and ionic contributions to bonding as well as solvent effects) and entropic contributions. The formation constants for a large number of hexadentate siderophores and bidentate model compounds are known.[4,8,10] The stability constant of $[Fe(cat)_3]^{3-}$ (cat = catecholate) is $10^{44.9}$, that of the hexadentate catecholate-based enterobactin is $10^{49}$, that of the tris-hydroxamate compound

[†] Department of Chemistry, Stanford University.
[‡] Monash University.
[§] Stanford Synchrotron Radiation Lightsource.
[#] Department of Chemistry, The University of California, Berkeley.
[⊥] Current address: Department of Chemistry and Chemical Biology, Baker Laboratory, Cornell University, Ithaca, NY 14853.

(1) Neilands J. B.; Konopka K.; Schwyn B.; Coy M.; Francis R. T.; Paw B. H.; Bagg A. *Iron Transport in Microbes, Plants and Animals*; VCH: Weinheim, 1987.
(2) Neilands, J. B. *J. Biol. Chem.* **1995**, *270*, 26723–26726.
(3) Codd, R. *Coord. Chem. Rev.* **2008**, *252*, 1387–1408.
(4) Raymond, K. N.; Dertz, E. A.; Sanggoo, S. *Proc. Natl. Acad. Sci. U.S.A.* **2003**, *100*, 3584–3588.
(5) Meyer, J. M.; Hohnadel, D.; Hall, F. *J. Gen. Microbiol.* **1989**, *135*, 1479–1487.
(6) Spasojevic, I.; Armstrong, S. K.; Brickman, T. J.; Crumbliss, A. L. *Inorg. Chem.* **1999**, 38.
(7) Carrano, C. J.; Dreschsel, H.; Kaiser, D.; Jung, G.; Berhold, M.; Wilnkelmann, G.; Rochel, N.; Albercht-Gray, A. M. *Inorg. Chem.* **1996**, *35*, 6429–6436.
(8) Dari-Abu K., B. S. J.; Riley, P. E.; Raymond, K. N. *Inorg. Chem.* **1983**, *22*, 3085–3089.
(9) Gerrett, T. M.; Miller, P. W.; Raymond, K. N. *Inorg. Chem.* **1989**, *28*, 128–133.
(10) Karpishin, R. B.; Gebhard, M. S.; Solomon, E. I.; Raymond, K. N. *J. Am. Chem. Soc.* **1991**, *113*, 2977–2984.
(11) Andreas, N. C. *N. Engl. J. Med.* **1999**, *342*, 1293–1294.
(12) Oliver, N. F.; Brittenham, G. M. *Blood* **1997**, *89*, 729–761.
(13) Esington, E. H.; Nishita, H. *Plant Soil* **2005**, *24*, 1–23.
(14) Chao, J. C.; Hong, A.; Okey, R. W.; Peters, R. W. *Proceedings of the Conference on Hazardous Waste Research*, Salt Lake City, UT, May 19−21, 1998; Great Plains/Rocky Mountain Hazardous Substance Research Center, Kansas State University: Manhattan, KS, 1998.

 **10.1021/ja9090098** 

$[Fe(aha)_3]$ ($aha^- =$ acetohydroxamate) is $10^{28.33}$, and that of the hexadentate tris-hydroxamate complex ferrioxamine B is $10^{30.6}$. Thus, both the catecholate and hydroxamate bidentate ligands make a significant contribution to the overall binding constants of the siderophores. For comparison, the stability constant[15] of the tris bidentate oxalate to form $[Fe(ox)_3]^{3-}$ is $10^{18}$. The bonding contributions to these differences in stability constants have been difficult to quantify experimentally.

Siderophores are generally brightly colored, due to low-energy ligand-to-metal charge-transfer (LMCT) transitions which reflect the very covalent nature of the ligand−metal bonds. In an earlier study,[10] we assigned these charge-transfer bands in $[Fe(cat)_3]^{3-}$ and could identify that the system had more $\pi$-donation than, for example, the analogous oxalate compounds, where LMCT transitions are absent at low energy. However, the magnitudes of $\pi$-donation and the relative magnitudes of $\pi$-donation to $\sigma$-donation cannot be extracted from charge-transfer bands.

Recently, a methodology has been developed based on L-edge X-ray absorption spectroscopy (XAS) coupled to multiplet simulations that enables the determination of the covalent delocalization of the different symmetry sets of d-orbitals, called differential orbital covalency (DOC).[16] The Fe L-edge, $2p \rightarrow 3d$ transition is electric dipole allowed, with the 2p-orbital localized on the Fe. This means that the Fe L-edge intensity is directly proportional to the Fe d-character in the valence orbitals on the metal, and thus the % metal character in the d-orbitals can be probed by the integrated L-edge intensity.[16−19] For systems where there is no back-bonding, a lower % metal character indicates a system that is more covalent. The shape of the spectrum gives insight into the ligand field but is complicated by multiplet contributions similar to the effects described by the Tanabe−Sugano[20] matrices and diagrams for $d^N$ metal complexes, but for the $2p^53d^{N+1}$ final states that also includes p−d electron repulsion and spin−orbit coupling. A further contribution to the L-edge shape is the effect of DOC. The effect of the differences in covalency on the different d-orbitals is now well understood in the case of Fe(III) low-spin complexes, where a distinct "$t_{2g}$ feature" is present on the low-energy side of the L-edge spectrum. The intensity of the "$t_{2g}$ feature" relative to the "$e_g$ feature" (a set of final state multiplets derived from the $2p^53d(t_{2g}^5e_g^1)$ configuration) further reflects the relative covalencies of the two symmetry sets of d-orbitals. Here, we study Fe L-edge XAS spectra of a series of high-spin compounds where the ligand field splitting is smaller than the electron−electron repulsion. This leads to a greater mixing of states, distributing the $\sigma$ and $\pi$ covalencies over the multiplets constituting the L-edge spectrum. It is found that the $\sigma$ and $\pi$ contributions can still be quantified experimentally from the spectral shape and correlated to DFT calculations, providing insight into electronic structure contributions to the high stability constants of the siderophores. The metal binding mode of each of the ligands included in this study, as well as bond lengths in Å, are given in Scheme 1.

***Scheme 1.*** Model Compounds Included in This Study[a]

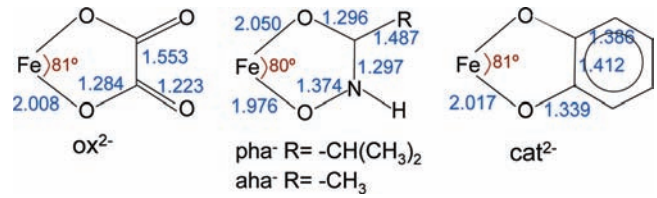


[a] Key distances are shown in Å.[21]

## 2. Experimental Section

**2.1. Sample Preparation.** $[Fe(pha)_3]$ and $K_3[Fe(cat)_3]$ (where cat = catecholate and pha = propyl-hydroxamate) were synthesized according to published methods.[22,23]

**2.2. XAS Data Collection.** X-ray absorption spectra were recorded at the Stanford Synchrotron Radiation Laboratory (SSRL) on the 31-pole wiggler beam line 10-1 and bending magnet beam line 8-2 (Fe L-edges), and on bending magnet beam line 2-3 (Fe K-edges), under ring operating conditions of 70−100 mA and 3 GeV. Details of the beam line optics have been described previously.[16,24] For Fe L-edge measurements, the samples were finely ground, spread across double-sided adhesive conductive graphite tape, and attached to a copper paddle, aligned 45° to the incident beam under an inert atmosphere.[25] All measurements were made at 20 ± 5 °C. The energy was calibrated from the Fe L-edge spectrum of $Fe_2O_3$, run at intervals between scans. The second feature in the $L_3$ and the first feature in the $L_2$ edges were calibrated to 708.5 and 720.1 eV, respectively. Data were taken over the range 670−830 eV to permit normalization, as described previously.[16] A step size of 0.1 eV was used over the edge region (700−730 eV), with 0.5 eV steps over the remaining regions. Two arc tangents were subtracted from the spectra to model the $L_3$ and $L_2$ edge jumps, as described previously:[16] absorption $= [\tan^{-1}(k(\text{energy} - I_1) + \pi/2)(2/3)1/\pi] + [\tan^{-1}(k(\text{energy} - I_2) + \pi/2)(1/3)(1/\pi)]$, where $k = 0.295$ was obtained from the experimental fit[16,26] and $I_2 = I_1 + 12.3$ eV (where $I_2$ is the energy of the $L_2$ feature relative to $I_1$ of $L_3$, split by spin−orbit coupling). The error reported represents the range of integrated intensity, based on at least three repeat measurements of the same spectra on different dates. For Fe K-edges the sample was mixed with boron nitride and ground into a fine powder. The powder was loaded into a 1 mm thick Al spacer and sealed with 63.5 $\mu$m Kapton tape windows. Fe K-edges were measured in transition mode with $N_2$-filled ionization chambers to $k = 9.5$ Å$^{-1}$. Two or three scans were measured per sample to ensure reproducibility. Energies were calibrated against the first inflection point at 7111.2 eV of an internal foil standard.[27] A second-order polynomial was fit to the pre-edge and subtracted from the data. A two-segment spline of order 2 was fit to the EXAFS region, and all data were normalized to the edge jump at 7130 eV.

(15) Deneux, M.; Meiller, R.; Benoit, R. L. *Can. J. Chem.* **1968**, *46*, 1383–1383.
(16) Wasinger, E. C.; deGroot, F. M. F.; Hedman, B.; Hodgson, K. O.; Solomon, E. I. *J. Am. Chem. Soc.* **2003**, *125*, 12894–12906.
(17) George, S. J.; Lowery, M. D.; Solomon, E. I.; Cramer, S. P. *J. Am. Chem. Soc.* **1993**, *115*, 2968–2969.
(18) Kotani, A.; Okada, K. *Tech. Rep. ISSP, Ser. A* **1992**, 2562.
(19) van der Laan, G.; Zaanen, J.; Sawatzky, G. A.; Karnatak, R.; Esteva, J. M. *Phys. Rev. B* **1986**, *33*, 4253–4263.
(20) Sugano S.; Tanabe Y. *Multiplets of transition-metal ions in crystals*; Academic Press: New York, 1970.
(21) Note that throughout, the MS data were taken on the tris propyl-hydroxamate complex of Fe, $[Fe(pha)_3]$, and that stability constant data and calculations are taken on the tris acetohydroxamate complex of Fe, $[Fe(aha)_3]$. The small difference between the two is illustrated inScheme 1.
(22) Abu-Dari, K.; Raymond, K. N. *J. Am. Chem. Soc.* **1977**, *99*, 2003–2005.
(23) Raymond, K. N.; Isied, S. S.; Brown, L. D.; Fronczek, F. R.; Nibert, J. H. *J. Am. Chem. Soc.* **1976**, *98*, 1767–1777.
(24) Westre, T. E.; Kennepohl, P.; DeWitt, J. G.; Hedman, B.; Hodgson, K. O.; Solomon, E. I. *J. Am. Chem. Soc.* **1997**, *119*, 6297–6314.
(25) DeBeer George, S.; Metz, M.; Szilagyi, R. K.; Wang, H.; Cramer, S. P.; Lu, Y.; Tolman, W. B.; Hedman, B.; Hodgson, K. O.; Solomon, E. I. *J. Am. Chem. Soc.* **2001**, *123*, 5757–5767.
(26) Yeh, J. J.; Lindau, I. *At. Data Nucl. Data Tables* **1985**, *32*, 1–155.
(27) Scott, R. A.; Hahn, J. E.; Doniach, S.; Freeman, H. C.; Hodgson, K. O. *J. Am. Chem. Soc.* **1982**, *104*, 5364–5369.

**2.3. Ligand Field Multiplet Calculations.** Calculations were performed using the multiplet model implemented by Thole,[28] which employs the atomic theory code developed by Cowan[29] and the crystal field (i.e., symmetry) code developed by Butler.[30] This approach includes both electronic Coulomb interactions and spin−orbit coupling for each subshell. To simulate the spectra, the Slater−Condon−Shortley parameters ($F_i$ and $G_i$) were first reduced to 80% of their Hartree−Fock calculated values to account for the overestimation of electron−electron repulsion found in *ab initio* Hartree−Fock calculations of the free ion. The spectrum is calculated from the sum of all possible transitions for an electron excited from the occupied 2p level into an unoccupied 3d level. In the crystal field limit, the ground state is given by a single electronic configuration $d^N$ (where $N$ = the number of valence d electrons), split in energy by electron repulsion and a ligand field potential in $O_h$ symmetry. The ligand field splitting of the d-orbitals is estimated from DFT calculated ground-state energies and eigenfunctions.

Covalent mixing of the metal valence d-orbitals with the ligand valence p-orbitals was included using a charge-transfer model which in the case of LMCT adds a $d^{N+1}\underline{L}$ configuration ($\underline{L}$ indicates a hole on the ligand) energetically above the $d^N$ ground configuration (by an energy separation $\Delta$). The two states are coupled by configuration interaction (CI), represented by the mixing term $T_i = \langle 3d^N|h|d^{N+1}\underline{L}\rangle$, where $h$ is the molecular Hamiltonian and $T_i$ is proportional to metal−ligand overlap for each of the $i$ symmetry blocks. For a donor ligand system the ground and LMCT states are $\Psi_{GS,B} = \alpha_1|3d^N\rangle + \beta_1|3d^{N+1}\underline{L}\rangle$ and $\Psi_{GS,AB} = \beta_1|3d^N\rangle - \alpha_1|3d^{N+1}\underline{L}\rangle$, and the L-edge excited states are $\Psi_{ES,B} = \alpha_2|\underline{2p}^5 3d^{N+1}\rangle + \beta_2|\underline{2p}^5 3d^{N+2}\underline{L}\rangle$ and $\Psi_{ES,AB} = \beta_2|\underline{2p}^5 3d^{N+1}\rangle - \alpha_2|\underline{2p}^5 3d^{N+2}\underline{L}\rangle$, where the coefficients $\alpha_1$, $\alpha_2$, $\beta_1$, and $\beta_2$ are functions of $T$ and $\Delta$ for the ground state and $T$ and $\Delta'$ for the excited state, where $\Delta' = \Delta_{GS} + U - Q$, $U$ being the 3d-3d electron repulsion and $Q$ is the 2p-3d repulsion. To simulate the spectra, first the combination of ligand field and multiplet effects was considered, and then $\sigma$- and $\pi$-donation were explicitly included by LMCT simulations.

In order to determine the DOC, the projection method of ref 16 was applied to the simulated spectrum. This method uses the TT-multiplets program to split the intensity of the spectrum into its different symmetry components via 4s→4p dummy transitions. These values are then degeneracy weighted to obtain the experimental DOC.

**2.4. DFT Calculations.** The starting structures of the compounds $[Fe(cat)_3]^{3-}$, $[Fe(aha)_3]$, $[Fe(ox)_3]^{3-}$, and $[Fe(F)_6]^{3-}$ (used as a reference for the stability constants, *vide infra*) were taken from the crystal structures of $K_3[Fe(cat)_3]\cdot 2H_2O$,[23] $[Fe(aha)_3]\cdot 2H_2O$,[31] $K_5Na[Fe(ox)_3]_2$,[32] and $[C(NH_2)_3]_3[Fe(F)_6]$,[33] respectively. DFT calculations were performed using both the ADF 2003 program[34−36] and Gaussian03 (revision C.01).[37] In ADF, the geometries were optimized using the exchange functional of Becke[38] and the correlation functional of Perdew (BP86).[39] The frozen core approximation[40] was used for the iron 1s-2p-orbitals. For valence orbitals, Slater-type orbital (STO) basis sets of triple-ζ quality were employed with polarization functions on the ligand atoms (3d) and additional valence p-orbitals on the metal atoms, i.e., ADF basis set IV.[35,36,41] This basis set combination has been shown to give a well-converged solution.[42,43] Mulliken population analysis was performed as implemented by ADF.[34] Orbital plots were generated using G-OpenMol version 2.2.[44] Inplicit solvation was applied in ADF, using the conductor-like screening model (COSMO).[33–35] Nonbonded radii used (in Å): N, 1.608; H, 1.350; C, 1.700; O, 1.517; and Fe, 1.750. A dielectric constant of 78.8 (water) and an outer cavity radius of 1.9 Å were further used to parametrize the COSMO solvation cavity.[45−47] For comparison, this process was repeated in Gaussian03 using the B3LYP exchange−correlation functional with the triple-ζ 6-311G** basis set and the polarized continuum model for solvation.[48−50] Molecular orbital (MO) compositions and overlap populations between molecular fragments were calculated using the AOMix program[51−54] or the QMForge (PyMolyze) program.[55]

To calculate stability constants, optimized geometries of all the components of the reaction were calculated using the B3LYP hybrid exchange−correlation functionals with the triple-ζ 6-311+G* basis set. This functional and basis set combination was found to reproduce the crystal structure of the model complexes and was used for further calculations. Total energies were obtained by single-point calculations on these structures using the B3LYP hybrid functional but with a larger 6-311++G** basis set. This improvement of the basis set did not change the energies by more than 1 kcal $mol^{-1}$. Tight SCF convergence criteria ($10^{-8}$ au) were used for all calculations. Frequency calculations were performed to ensure that stationary points were minima. The molar entropy, enthalpy, and Gibbs free energy of reaction at 298 K and at a pressure of 1 atm were calculated using standard statistical mechanics formulas.[56]

## 3. Results

**3.1. Spectroscopy. 3.1.1. Fe K-Edge Spectra.** Figure 1 shows the normalized Fe K-edge spectra of $K_3[Fe(ox)_3]$, $[Fe(pha)_3]$,[21] and $K_3[Fe(cat)_3]$. The energy shift of the rising edge follows the trend $K_3[Fe(cat)_3] < [Fe(pha)_3] < K_3[Fe(ox)_3]$. An expansion


(28) Thole, B. T.; van der Laan, G.; Fuggle, J. C.; Sawatzky, G. A.; Karanatak, R. C.; Esteva, J.-M. *Phys. Rev. B.* **1985**, *32*, 5107–5118.
(29) Cowan, R. D. *The Theory of Atomic Structure and Spectra*; University of California Press: Berkeley, CA, 1981.
(30) Butler, P. H. *Point Group Symmetry, Applications, Methods and Tables*; Plenum Press: New York, 1991.
(31) Failes, T. W.; Hambley, T. W. *Aust. J. Chem.* **2000**, *53*, 879–881.
(32) Wartchow, R. *Z. Kristallogr.* **1997**, *212*, 57–58.
(33) Fourquet, J. L.; Plet, F. Y. C.; De Pape, R. *J. Solid State Chem.* **1987**, *69*, 76–80.
(34) Mulliken, R. S. *J. Chem. Phys.* **1955**, *23*, 1833–1840.
(35) *Scientific Computing and Modeling (SCM)*, ADF User's Guide; Theoretical Chemistry, Vrije Universiteit: Amsterdam, The Netherlands, 2003.
(36) BaerendsE. J.; et al. *ADF*, 2003.01, SCM; Theoretical Chemistry, Vrije Universiteit: Amsterdam, The Netherlands, 2003; http://www.scm.com
(37) FrischM. J.; et al. *Gaussian 03*, Revision 01; Gaussian Inc.: Wallingford, CT, 2003.
(38) Becke, A. D. *Phys. Rev. A* **1988**, *38*, 3098–3100.
(39) Perdew, J. P. *Phys. Rev. B* **1986**, *33*, 8822–8824.
(40) Baerends, E. J.; Ellis, D. E.; Ros, P. *Theor. Chim. Acta* **1972**, *27*, 339–354.
(41) Te Velde, G.; Baerends, E. J.; Fonseca, G. C.; Van Gisbergen, S. J. A.; Snijders, J. G.; Ziegler, T. *J. Comput. Chem.* **2001**, *22*, 931–967.
(42) Ryde, U.; Olsson, M. H. M.; Pierloot, K. *Theoretical and Computational Chemistry*; Elsevier: Amsterdam, 2001; Vol. 9, pp 1−55.
(43) Siegbahn, P. E. M.; Blomberg, M. R. A. *Chem. Rev.* **2000**, *100*, 421–437.
(44) http://www.csc.fi/gopenmol/distribute/index.phtml.
(45) Klamt, A. *J. Chem. Phys.* **1995**, *99*, 2224.
(46) Klamt, A.; Jones, V. *J. Chem. Phys.* **1996**, *105*, 9972.
(47) Klamt, A.; Schuurmann, G. *J. Chem. Soc., Perkin Trans. 2* **1993**, 799.
(48) Mennucci, B.; Cances, E.; Tomasi, J. *J. Phys. Chem. B* **1997**, *101*, 10506–10507.
(49) Cammi, R.; Mennucci, B.; Tomasi, J. *J. Phys. Chem. A* **1999**, *103*, 9100–9102.
(50) Cammi, R.; Mennucci, B.; Tomasi, J. *J. Phys. Chem. A* **2000**, *104*, 5631–5632.
(51) Lever, A. B. P.; Gorelsky, S. I. *Struct. Bonding (Berlin)* **2004**, *107*, 77–114.
(52) Gorelsky, S. I.; Basumallick, L.; Vura-Weis, J.; Sarangi, R.; Hodgson, K. O.; Hedman, B.; Fujisawa, K.; Solomon, E. I. *Inorg. Chem.* **2005**, *44*, 4947–4960.
(53) Gorelsky, S. I. *AOMix program*, rev. 5.93, 2004; http://www.sg-chem.net/.
(54) Gorelsky, S. I.; Lever, A. B. P. *J. Organomet. Chem.* **2001**, *635*, 187–196.
(55) Tenderholt, A. L.; Hodgson, K. O.; Hedman, B.; Solomon, E. I. *QMForge*, a program for the analysis of MO coefficients; Stanford University: Stanford, CA, 2005; http://pymolyze.sourceforge.net.
(56) Atkins, P. W. *Physical Chemistry*, 3rd ed.; Oxford University Press: Oxford, UK, 1986.

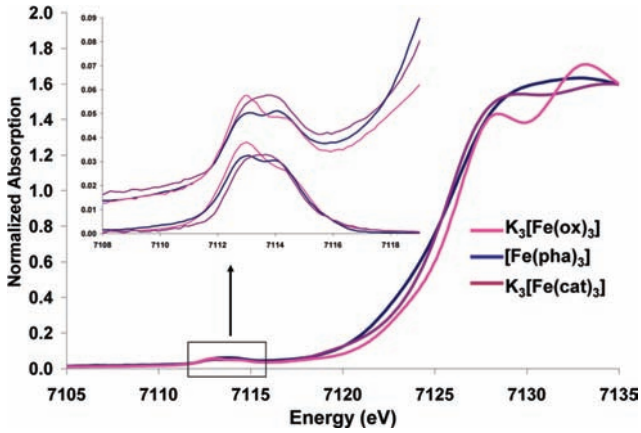


***Figure 1.*** Comparison of the Fe K-edge data for the compounds $K_3[Fe(ox)_3]$ (data from ref 25), $[Fe(pha)_3]$, and $K_3[Fe(cat)_3]$. The inset expands the pre-edges, with upper spectra showing the experimental data and lower the background-subtracted data.

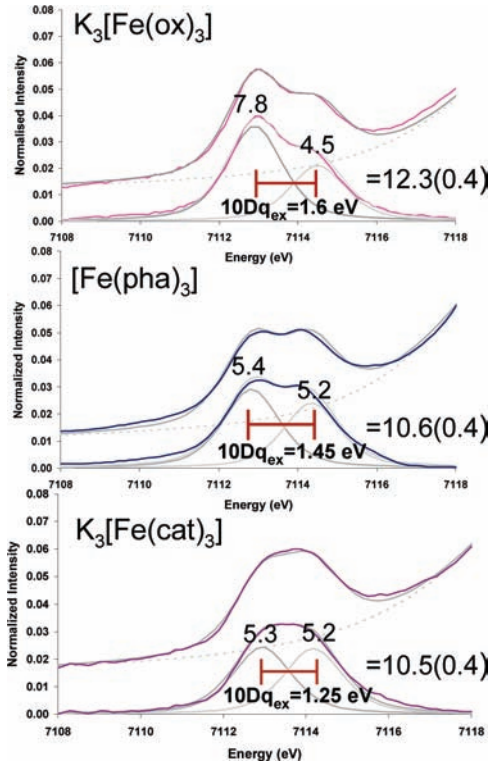


***Figure 2.*** Fits to the Fe K pre-edge data for the compounds $K_3[Fe(ox_3)]$, $[Fe(pha)_3]$, and $K_3[Fe(cat)_3]$. In each frame the upper spectrum (colored) shows the data, and the lower spectrum shows the background-subtracted fit to the data.

of the energy region 7109−7119 eV is given in the inset, along with the background subtracted pre-edges. In all cases, the pre-edge spectra were fit with two pseudo-Voigt functions, Figure 2 (see also Supporting Information, Table S1). The energy difference between the two peaks follows the trend $K_3[Fe(cat)_3] < [Fe(pha)_3] < K_3[Fe(ox)_3]$. The pre-edge intensities of the three compounds are slightly different, with that of oxalate being 1.8 units more intense than those of hydroxamate and catecholate complexes, the difference in intensity coming predominantly from the lower energy peak.

**3.1.2. Fe L-Edge Spectra.** Figure 3 shows the normalized Fe L-edge spectra of $K_3[Fe(ox)_3]$, $[Fe(pha)_3]$, and $K_3[Fe(cat)_3]$. The inset compares the three spectra shifted in energy and scaled

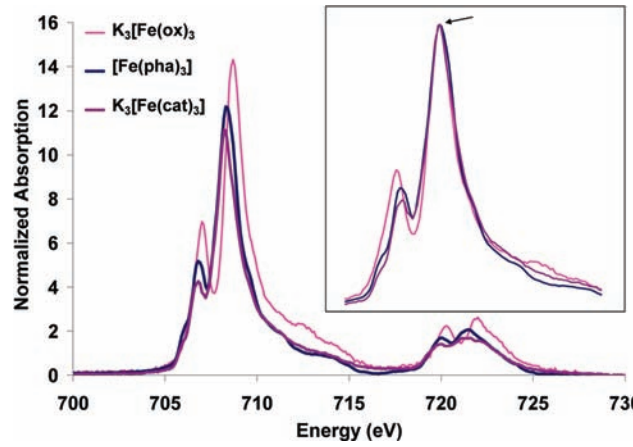


***Figure 3.*** Normalized Fe L-edge absorption spectra for the compounds $K_3[Fe(cat)_3]$, $[Fe(pha)_3]$, and $K_3[Fe(ox)_3]$ (data from ref 16). The inset shows the three spectra shifted in energy to superimpose and scaled to the same intensity on the main peak, indicated with an arrow.

so that the main feature of each is superimposed. The change in total intensity corresponds to a change in the total metal d-character in the unoccupied orbitals, which increases across the series $K_3[Fe(cat)_3]$ 65(5) < $[Fe(pha)_3]$ 68(5) < $K_3[Fe(ox)_3]$ 84(5) (see Table 1). The superimposed spectra (Figure 3, inset) show a systematic change in shape. The intensity of the lowest energy spectral feature increases across the series $K_3[Fe(cat)_3] < [Fe(pha)_3] < K_3[Fe(ox)_3]$ such that the ox spectrum has the two most pronounced features, and in the catecholate spectrum the first feature is shifted up in energy and decreased in intensity to a shoulder on the main peak.

**3.2. Analysis. 3.2.1. Fe K-Edge Spectra.** The Fe K pre-edge spectra of high-spin $Fe^{III}$ compounds in Figure 2 show two peaks that reflect Fe 1s→3d transitions producing $^5T_2$ and $^5E$ states (which equivalently couple to the $(1s)^1$, $^2S$ core hole) split by an excited state 10Dq ($10Dq_{ex}$).[24] The magnitude of $10Dq_{ex}$ decreases across the series $[Fe(ox)_3]^{3-}$ (1.60 eV) > $[Fe(pha)_3]$ (1.45 eV) > $[Fe(cat)_3]^{3-}$ (1.25 eV), consistent with an increase in $\pi$ donation or a decrease in $\sigma$ donation (however, the $\sigma$ donation in fact increases, *vide infra*). The values of $10Dq_{ex}$ are smaller than those values obtained from optical data for $[Fe(cat)_3]^{3-}$ (1.30 eV)[10] and $[Fe(ox)_3]^{3-}$ (1.75 eV),[58] consistent with observations by Cramer et al.[59] that $10Dq_{ex}$ is smaller than 10Dq of transitions within the ground configuration. From Figure 2, the intensity of the $K_3[Fe(ox)_3]$ spectrum is 1.8(0.4) units higher than those of the $[Fe(pha)_3]$ and $K_3[Fe(cat)_3]$ compounds, with the difference being predominantly attributable to the first feature ($^5T_2$). There are two mechanisms for intensity at an Fe K pre-edge. The first is the direct quadrupole-allowed transition to the Fe 3d-orbitals, whose intensity is affected by covalency. The second is the electric dipole transition to the small amount of Fe 4p character mixed into the Fe 3d-orbitals, which increases with deviations from centrosymmetry.[24] It has been shown that, for Fe(III), ∼6−7 units of intensity are due to the to the quadrupole-allowed Fe 1s→3d character, with the remainder of the pre-edge intensity being attributed to the electric dipole-allowed Fe 1s→4p character. All three com-

(57) Thole, B. T.; van der Laan, G. *Phys. Rev. B* **1988**, *38*, 3158–3170.
(58) Figgis, B. N.; Hitchman, M. A. *Ligand Field Theory and Its Applications*; Wiley-VCH: Weinheim, 2000.
(59) Wang, H.; Peng, G.; Miller, L. M.; Scheuring, E. M.; George, S. J.; Chance, M. R.; Cramer, S. P. *J. Am. Chem. Soc.* **1997**, *119*, 4921–4928.

**Table 1.** Summary of Fe L-Edge Data for the Series of Compounds $K_3[Fe(ox)_3]$, $[Fe(pha)_3]$, and $K_3[Fe(cat)_3]$

| | $L_3$ intensity, 702−717 eV | intensity-weighted average energy ($L_3$) | $L_2$ intensity, 717−727 eV | intensity-weighted average energy ($L_2$) | branching ratio $I(L_3)/I(L_2 + L_3)$ | average % d character in unoccupied orbitals[a] |
|---|---|---|---|---|---|---|
| $K_3[Fe(ox)_3]$ | 41.6 | 709.4 | 10.4 | 721.7 | 0.80 | 84(5) |
| $[Fe(pha)_3]$ | 33.6 | 708.9 | 7.9 | 721.4 | 0.81 | 68(5) |
| $K_3[Fe(cat)_3]$ | 31.3 | 709.2 | 7.9 | 721.3 | 0.80 | 65(5) |

[a] Note that the % metal d character is inversely proportional to the covalency.

pounds studied here have O−Fe−O angles of 80° (Scheme 1), and the 4p mixing is calculated to be similar (~0.5% from the calculations presented in section 3.2.2.3), indicating that the higher intensity in oxalate relative to catecholate and hydroxamate is attributable to differences in valence metal d character, with the oxalate complex having a higher % metal d character, therefore being less covalent. The difference in intensity of the first feature relative to the second when comparing oxalate to catecholate and hydroxamate is consistent with the trends in $10Dq_{ex}$ and indicates that the $\pi$ ($t_{2g}$) covalency difference of the series is larger than that of the d $\sigma$($e_g$) orbitals.

**3.2.2. Fe L-Edge Spectra. 3.2.2.1. Total Intensity and Energy.** Three aspects of Fe L-edge spectra are consequences of bonding: total intensity, energy shift, and spectral shape. Comparing the compounds $K_3[Fe(ox)_3] \rightarrow [Fe(pha)_3] \rightarrow K_3[Fe(cat)_3]$, the total intensity decreases (Table 1), indicating that the average ligand character, and therefore the covalency, of the unoccupied metal d-based orbitals increases. Metal L-edge energy shifts reflect three contributions: the charge on the absorbing metal atom in the molecule, the ligand field splittings of the d-orbitals, and any difference in the nature of the ligand valence orbitals. The last contribution is important: metal character mixed into low-lying $\pi$* ligand-based orbitals due to back-bonding will increase the intensity and change the energy/intensity distribution of a spectrum.[60,61] In the case of high-spin Fe(III), the contribution of the ligand field should be negligible, as the degeneracy-weighted average energy of the d-orbitals is zero. As there will also be no spectroscopic contribution from $\pi$*-orbitals for the donor ligands studied herein, we expect little energy shift, and indeed the intensity-weighted energies of the L-edge spectra of these complexes are the same within error (Table 1). Note that this is in contrast to low-spin ferric systems, where an energy difference of up to 1.4 eV due to the ligand field is observed.[60]

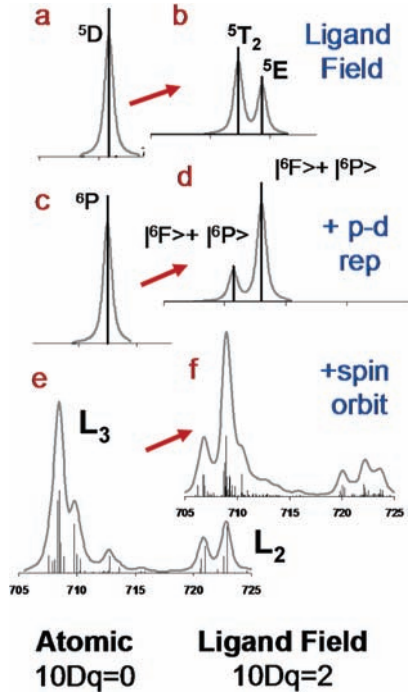


***Figure 4.*** Systematic inclusion of multiplet contributions to the L-edge spectrum of high-spin Fe(III), left for free ion, right for $O_h$ metal complex. (a,b) Spectra in the absence of spin−orbit or p−d repulsion. (c,d) Spectra including the effects of p−d repulsion.[62] (e,f) Spectra also including spin−orbit coupling, from $L_3$, $J = {}^3/_2$ and from $L_2$, $J = {}^1/_2$.

***Table 2.*** Free Ion →$O_h$ complex

| | O |
|---|---|
| S | $A_1$ |
| P | $T_1$ |
| D | $E + T_2$ |
| F | $A_2 + T_1 + T_2$ |

**3.2.2.2. Spectral Shape.** The L-edge spectral shape has three contributions: electrostatic multiplet effects, ligand field effects, and differential orbital covalency. These will be systematically evaluated below for these high-spin $Fe^{III}$ complexes.

**3.2.2.2-a. Multiplet and Ligand Field Effects on Spectral Shape.** In the absence of covalency, the spectral shape has contributions from d−d repulsion, p−d repulsion, spin−orbit coupling, and the ligand field splitting of the d-orbitals. The effect on the Fe L-edge of each of these contributions is given in Figure 4. Spectrum a shows the single state that would result when no multiplet effect is present; spectrum b results from the effect of an $O_h$ ligand field on high-spin Fe(III), i.e., two peaks with intensity ratio of 3:2. These are the $^5T_2$ and $^5E$ states on the weak-field side of a $d^6$ final state Tanabe−Sugano diagram (no coupling to the $^2P$ ($2p^5$) core hole). Spectra c and d take into account the 2p core hole ($^2P$). When this is coupled with the $^5D$ ($3d^6$ free ion term symbol), three sextet states arise, $^6F + {}^6D + {}^6P$, and only the transition to the $^6P$ is electric dipole allowed from the $^6S$ ground state. However, with an $O_h$ ligand field (Figure 4, c→d) the $^6F$ state mixes with the $^6P$ because both of these states have a $T_1$ symmetry component (Table 2). The energy separation between these two states is a function of p−d repulsion and, to some extent, the magnitude of the ligand field. At low 10Dq, there is little intensity in the $^6F$ state, and the two states are separated by p−d repulsion (1.2 eV). However, as 10Dq gets large, the splitting of these two states becomes dominated by 10Dq. Upon the addition of spin−orbit coupling, the states split further; however, the shape and

(60) Hocking, R. K.; Wasinger, E. C.; deGroot, F. M. F.; Hodgson, K. O.; Hedman, B.; Solomon, E. I. *J. Am. Chem. Soc.* **2006**, *128*, 10442–10451.
(61) Sarangi, R.; Nermeen, A.; Fujisawa, K.; Tolman, W. B.; Hedman, B.; Hodgson, K. O.; Solomon, E. I. *J. Am. Chem. Soc.* **2006**, *128*, 8286–8296.

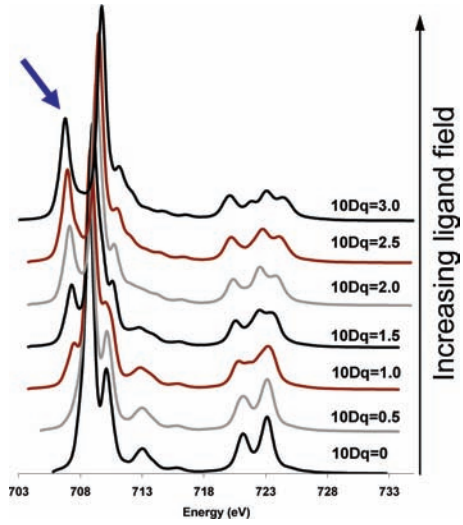


***Figure 5.*** Calculated effect of ligand field on the spectrum of high-spin Fe(III) complex. Top spectrum, 10Dq = 3.0 eV; bottom spectrum, 10Dq = 0. Arrow indicates the prominent low-energy feature that appears as 10Dq increases.

separation of the $|^6F\rangle$ and $|^6P\rangle$ dominate the $L_3$ and $L_2$ spectral shapes (Figure 4f). Note that of the two contributions to spin−orbit coupling, 2p dominates (Supporting Information, Figure S4).

**3.2.2.2-b. Systematic Evaluation of 10Dq.** Figure 5 shows the effect of systematically increasing 10Dq from the atomic limit (10Dq = 0 eV) to 10Dq = 3.0 eV, all complexes having a high-spin ground state. It is clear that as 10Dq is increased, the spectra get broader and begin to take on features analogous to those in Figure 4f. A prominent feature that appears as 10Dq increases is the peak on the low-energy side of the $L_3$, indicated by the arrow in Figure 5.

While the compounds studied here are $D_3$ distorted from $O_h$, the distortions are small relative to the other contributions to the state splitting and do not impact on spectral shape.[10] The difference between $O_h$ symmetry simulations and low-symmetry simulations is given in Supporting Information, Figure S5.

**3.2.2.2-c. Differential Orbital Covalency.** In order to determine the difference in $\pi$ and $\sigma$ d character distributed over the L-edge, the spectrum in Figure 6 (10Dq = 1.8 eV but now including equal amounts of $\sigma$ and $\pi$ covalency) was generated (Figure 6, isotropic spectrum, gray). Further spectra were generated with only $\pi$ covalency and only $\sigma$ covalency, but with 80% total hole-weighted orbital covalency. These spectra are shown in the Supporting Information, Figure S2. These spectra were subtracted and renormalized to obtain pure $\pi$ (Figure 6, blue) and $\sigma$ (Figure 6, pink) density-of-state distributions across the high-spin Fe(III) L-edge spectrum. This methodology is presented in more detail in the Supporting Information.

While both the $\sigma$ and $\pi$ contributions are clearly distributed over all parts of the L-edge, there is a higher proportion of $\pi$ relative to $\sigma$ character in the low-energy feature (arrow in Figure 6). This difference in distribution enables a determination of the DOC. A stronger $\pi$ contribution to bonding will lead to lower intensity in the first feature relative to the large peak at 710 eV.

**3.2.2.2-d. Fits to Data.** From the experimental spectra given in Figure 3, on going from $[Fe(ox)_3]^{3-}$ to $[Fe(pha)_3]$ to

(62) Note that for high-spin Fe(III) d−d repulsion does not cause any additional splitting.

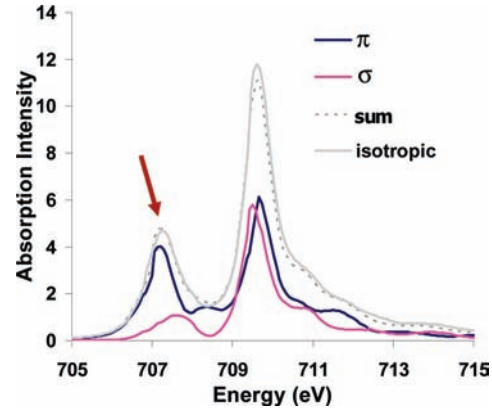


***Figure 6.*** $\sigma$ and $\pi$ density of states for an $O_h$ Fe(III) high-spin $L_3$-edge with 10Dq = 1.8 eV.

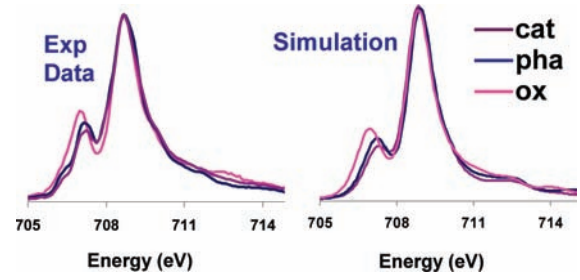


***Figure 7.*** Comparison of valence bond configuration interaction (VBCI) simulation and experiment (inset in Figure 1) for Fe $L_3$ edge of the series $K_3[Fe(ox)_3]$, $[Fe(pha)_3]$, and $K_3[Fe(cat)_3]$.

***Table 3.*** Parameters Used in VBCI Simulations[a]

| spectrum | EG2 | EF2 | $\Delta_0$ | $T(e_g)$ | $T(t_{2g})$ | 10Dq |
|---|---|---|---|---|---|---|
| $K_3[Fe(ox)_3]$ | 1 | −1 | 1.51 | 1.8 | 0.8 | 1.5 |
| $[Fe(pha)_3]$ | 1 | −1 | 1.45 | 2.0 | 1.2 | 1.3 |
| $K_3[Fe(cat)_3]$ | 0 | −2 | 0.27 | 1.6 | 1.0 | 1.3 |

[a] EG2 is the separation of the two lowest energy states in each configuration in the ground/initial state; EF2 is this separation in the final state. $\Delta_0$ is the weighted average energy separation of these states in the initial state. $T(e_g)$ and $T(t_{2g})$ are the mixing terms (*vide supra*).

$[Fe(cat)_3]^{3-}$, the first feature decreases in intensity relative to the second, and the two peaks are shifted closer together. From the above analysis, this is indicative of a decrease in 10Dq and an increase in $\pi$ donation. The simulations of the experimental data are given in Figure 7 and compared to the experimental spectra (full simulations including the $L_2$ pre-edge are given in Supporting Information, Figure S6). The dominant parameter that needed to be varied to simulate the spectral changes was the $t_{2g}$ mixing ($\pi$ donation); however, a decrease in 10Dq across the series was also necessary (Table 3). To interpret the simulations in terms of experimental estimates of MO coefficients, it is necessary to project the symmetry components as described previously.[16] The results of these projections are given in Table 4, columns 4−6. The experiment shows a substantial increase in $\pi$ donation across the series, from limited $\pi$ donation in ferric tris-oxalate (6%) to substantial $\pi$ donor character in ferric catecholate (26%) (Table 4). The $\sigma$ covalency also increased, particularly in the catecholate system.

**3.2.2.3. Comparison to DFT. 3.2.2.3-a. Geometry Optimization.** Geometry optimizations of all compounds were performed

(63) Population analysis was done using $C^2$.

***Table 4.*** Summary of L-Edge Integrated Intensity, Average Experimental Covalency (Given as d Character in Unoccupied Orbitals), Differential Orbital Covalency (DOC), and DFT Calculations

| | | | projected experimental covalency | | | DFT (BP86)[63] | | | | DFT (B3LYP)[63] | | | |
|---|---|---|---|---|---|---|---|---|---|---|---|---|---|
| species | intensity | average % d character in unoccupied orbitals[a] | Fe ($t_{2g}$) $\pi$ | Fe ($e_g$) $\sigma$ | DOC | avg | Fe ($t_{2g}$) | Fe ($e_g$) | DOC | avg | Fe ($t_{2g}$) | Fe ($e_g$) | DOC |
| $[Fe(ox)_3]^{3-}$ | 53.3(4.0) | 84(5) | 94 | 69 | 25 | 72 | 80 | 61 | 19 | 80 | 88 | 69 | 19 |
| $[Fe(pha)_3]$ | 43.1(3.6) | 68(5) | 72 | 61 | 11 | 62 | 63 | 60 | 3 | 70 | 74 | 64 | 10 |
| $[Fe(cat)_3]^{3-}$ | 41.2(3.1) | 65(5) | 74 | 52 | 22 | 56 | 62 | 46 | 16 | 63 | 74 | 50 | 24 |

[a] Note that the % metal d character is inversely proportional to the covalency.

***Table 5.*** Comparison of Calculated and Experimental Thermodynamic Parameters Values in Water unless Otherwise Indicated

| | $K_{STAB}$(exp) $[FeF_6]^{3-}$ + 3L ↔ $[FeL_3]$ + 6F$^-$ | $\Delta G$(exp), 298 K | $\Delta H$(calc) | $T\Delta S$(calc) | $\Delta G$(calc), 298 K | $\Delta G$(calc, gas phase), 298 K |
|---|---|---|---|---|---|---|
| $[Fe(ox)_3]^{3-}/[Fe(F)_6]^{3-}$ | $10^{18.49}/10^{15.04}$ | −4.6 | 17.3 | 10.1 | 7.2 | 67.4 |
| $[Fe(aha)_3]^{3-}/[Fe(F)_6]^{3-}$ | $10^{28.33}/10^{15.04}$ | −18.14 | 8.8 | 12.3 | −3.4 | 193.0 |
| $[Fe(cat)_3]^{3-}/[Fe(F)_6]^{3-}$ | $10^{44.9}/10^{15.04}$ | −40.8 | −18.4 | 6.5 | −25.0 | 38.4 |

using BP86 and B3LYP. The geometric structure parameters are compared to experiment in the Supporting Information, Table S2. In general, the optimized structures agree well with the experiment; however, the Fe−O bond lengths are uniformly too long across the series of compounds, consistent with what has been noted elsewhere.[64,65]

**3.2.2.3-b. Differential Orbital Covalency.** Table 4 compares the calculated values of total orbital covalency and DOC to experiment. The trends in total orbital covalency are oxalate → hydroxamate → catecholate: experiment (% d character), 84 → 68 → 65; B3LYP, 80 → 70 → 63; BP86, 72 → 62 → 56. These indicate that the magnitude of the trend is better reproduced with the B3LYP hybrid functional, as BP86 describes the complexes as overly covalent. The analogous comparisons for DOC (difference in $\pi$ vs $\sigma$ contribution) oxalate → hydroxamate → catecholate are: experiment (25 → 11 → 22); B3LYP (19 → 10 → 24); BP86 (19→ 3 → 16). These also indicate a better agreement between experiment and the B3LYP calculation.

**3.2.2.3-c. Stability Constants.** As the B3LYP calculations gave electronic structure descriptions most consistent with experiment, they were chosen for further analysis of stability constant data. The experimental numbers for the tris-ligand binding to $[Fe(H_2O)_6]^{3+}$ are $10^{44.9}$ for $[Fe(cat)_3]^{3-}$,[66,67] $10^{28.3}$ for $[Fe(aha)_3]$,[68] and $10^{18.49}$ for $[Fe(ox)_3]^{3-}$.[68] These are corrected for p$K_a$ effects and are therefore appropriate for comparison. Calculations of $[Fe(H_2O)_6]^{3+}$ are complicated by intramolecular H-bonding effects due to modeling in a PCM; therefore, $[FeF_6]^{3-}$ was chosen as a reference. In order to compare the calculated thermodynamic values to experiment, the measured stability constants of the reactions referenced against $[Fe(H_2O)_6]^{3+}$ were converted to $[FeF_6]^{3-}$ as a reference ($10^{15.04}$), giving the ratios in Table 5, column 2.[21] The calculations in solvent next to last column) reproduce the experimental trends in stability constants, with the $\Delta G$ of hydroxamate being ∼10 kcal/mol more negative than for oxalate, and that of catecholate being ∼20 kcal/mol more favorable than for hydroxamate. The $T\Delta S$ components giving the entropic contributions do not vary much across this series of compounds. Thus, the differences in $\Delta G$ across the series are dominantly due to the $\Delta H$ contributions to bonding and are examined below.

***Table 6.*** NPA Charge Distributions Gas (Solvated) for $[Fe(ox)_3]^{3-}$, $[Fe(aha)_3]$, and $[Fe(cat)_3]^{3-}$ [a]

| | $[Fe(ox)_3]^{3-}$ | $[Fe(aha)_3]$ | $[Fe(cat)_3]^{3-}$ |
|---|---|---|---|
| Fe | 1.98 (1.98) | 1.91 (1.90) | 1.95 (1.92) |
| ligand | −1.66 (−1.66) | −0.64 (−0.63) | −1.65 (−1.64) |
| O | −0.81 (−0.83) | −0.71 (−0.75) | −0.81 (−0.87) |

[a] Fe is the charge on the Fe in each complex, ligand is the average charge on the bidentate ligand, and O gives the average charge on the O bound to Fe.

Gas-phase values for $\Delta G$ are given in the final column of Table 5. The trend for oxalate and catecholate is similar in both the solvent and gas-phase calculations. Therefore, this difference between oxalate and catecholate binding is dominated by differences in the ionic and covalent contributions to bonding. To examine the ionic contribution, natural population analysis (NPA) charge distributions were calculated in both the gas and solvated phases (Table 6). From the NPA charge distributions, oxalate has a slightly larger ionic term than catecholate. Therefore, the difference in $\Delta G$ has its origin in the difference in covalent contributions to bonding revealed by the L-edge data in Figure 3 and Table 4, i.e., the high $\pi$ and $\sigma$ covalency of the cat−Fe(III) bond relative to ox. Examination of the $\Delta G$ for hydroxamate reveals a large difference in calculated gas- vs condensed-phase values. Hydroxamate bonding is significantly less favorable in the gas phase, indicating a substantially weaker Fe(III)−hydroxamate bond. From the L-edge data in Table 4, the covalency of hydroxamate is, in fact, significantly higher than that of ox. However, from Table 6, hydroxamate has a substantially reduced ionic contribution to bonding. In the solvated phase this is more than compensated by the decreased solvation of the monoanionic hydroxamate relative to the dianionic catecholate and oxalate ligands (Table 5).

To evaluate the iron 3d-orbital contributions to the stability constants of the tris ox, aha, and cat complexes, it is useful to make a comparison to analogous compounds of Al and Ga. A tabulation of the experimental stability constants is given in Table 7. The results from parallel calculations are in good

(64) Bray, M. R.; Deeth, R. J.; Paget, V. J.; Sheen, P. D. *Int. J. Quantum Chem.* **1996**, *61*, 85–91.
(65) Hocking, R. K.; Deeth, R. J.; Hambley, T. W. *Inorg. Chem.* **2007**, *46*, 8238–8244.
(66) Motekaitis, R. J.; Martell, A. E. *Inorg. Chim. Acta* **1991**, *183*, 71–80.
(67) Avdeef, A.; Sofen, S. R.; Bregante, T. L.; Raymond, K. N. *J. Am. Chem. Soc.* **1978**, *100*, 5362–5370.
(68) Smith, R. M.; Martell, A. E. *Critical Stability Constants*; Plenum Press: New York, 1974; Vol. 3.
(69) Stary, J. *Anal. Chim. Acta* **1962**, *28*, 132–149.
(70) Fein, J.; Hestrin, J. E. *Geochim. Cosmochim. Acta* **1994**, *58*, 4817–2829.
(71) Burgess, J.; Patel, M. S. *J. Coord. Chem.* **1993**, *29*, 65–71.
(72) Farkas, E.; Kozma, E.; Kiss, T.; Toth, I.; Kurzak, B. *J. Chem. Soc., Dalton. Trans.* **1995**, 477–480.

***Table 7.*** Stability Constant Data Available in the Literature from tris ox, aha, and cat Coordinated to Fe(III), Ga(III), and Al(III)

| | Fe(III) | Ga(III) | Al(III) |
|---|---|---|---|
| $[M(ox)_3]^{3-}$ | $10^{18}$ | $10^{17.98}$[a] | $10^{18.1}$[b] |
| $[M(aha)_3]$ | $10^{28.33}$ | $10^{26.21}$[c] | $10^{21.5}$[c] |
| $[M(cat)_3]^{3-}$ | $10^{44.9}$ ($10^{46}$)[d] | ($10^{45.5}$)[d] | $10^{37.95}$[e] |

[a] Reference 69. [b] Reference 70. [c] Reference 71. [d] This number is based on a close analogue of catecholate, Tiron.[73] [e] Reference 72.

***Table 8.*** Analysis of Unoccupied Metal Character in Occupied Orbitals

| | 4s (Ga, Fe)/3s (Al) | 4p(Fe, Ga)/3p (Al) | 3d |
|---|---|---|---|
| $[Fe(ox)_3]^{3-}$ | $\alpha$ 35 | $\alpha$ 5.3 | 116% |
| | $\beta$ 31.3 | $\beta$ 5.3 | (62% $\sigma$; 54% $\pi$) |
| $[Al(ox)_3]^{3-}$ | 37.2 | 25.8 | 0 |
| $[Ga(ox)_3]^{3-}$ | 48.0 | 29.8 | 0 |
| $[Fe(aha)_3]$ | $\alpha$ 29 | $\alpha$ 6.0 | 150% |
| | $\beta$ 27 | $\beta$ 5.5 | (72% $\sigma$; 78% $\pi$) |
| $[Al(aha)_3]$ | 35.9 | 25.9 | 0 |
| $[Ga(aha)_3]$ | 48 | 28.9 | 0 |
| $[Fe(cat)_3]^{3-}$ | $\alpha$ 36 | $\alpha$ 8.3 | 178% |
| ($\alpha + \beta$) | $\beta$ 33 | $\beta$ 8.1 | (100% $\sigma$; 78% $\pi$) |
| $[Al(cat)_3]^{3-}$ | 43 | 36.7 | 0 |
| $[Ga(cat)_3]^{3-}$ | 56 | 40.9 | 0 |

agreement with the experimental data and are given in Supporting Information, Table S3.

The tris ox complexes of Fe and Ga have similar stability constants, both $\sim 10^{18}$. From the NPA (Supporting Information, Table S4), Ga is at least as covalent as Fe. To analyze the origin of this covalency, the amount of unoccupied metal character mixed into occupied orbitals is given in Table 8. This comparison indicates that Ga has substantially more 4s/4p character involved in ligand donor bonding than Fe (48 vs 33% 4s, and 30 vs 5% 4p). However, this difference in 4s/4p covalency is compensated by the substantial donation into the Fe 3d-orbitals which is absent in Ga. Comparing ox to cat, the stability constants of both Ga and Fe increase by 27 orders of magnitude. In both Ga and Fe, the mixing of unoccupied 4s/4p character into occupied ligand orbitals increases; however, for Fe this difference is more limited (Ga, from 48 to 56% 4s and from 26 to 41% 4p; Fe, from 33 to 35% 4s and from 5 to 8% 4p). As for the ox metal bonds, the substantial difference in the increase between donation into the 4s- and 4p-orbitals is compensated for in Fe by the substantial increased donation into the 3d-orbitals from 116 to 178%, which is absent in Ga, leading to their similar stability constant increases.

While the Al and Ga both have very similar stability constants with ox, the stability constants for Al do not increase by the same magnitude on going from aha to cat. There is a 5 orders of magnitude separation between Al and Ga for aha and an 8 orders of magnitude difference for cat. From Table 8 it can be seen that Al is consistently less covalent than Ga, paralleling their differences in stability constants.

## 4. Discussion

**4.1. Weak Field and Strong Field Effects on L-Edge Spectral Shape.** In order to interpret DOC from the L-edge spectral shape, it is necessary to identify regions of the spectrum that are dominated by transitions to the different symmetry sets of orbitals, $t_{2g}(\pi)$ and $e_g(\sigma)$ in $O_h$. The spectral shape at an L-edge is strikingly different for the different spin states. Representative L-edge spectra of low-spin and high-spin Fe(III) are given in Figure 8, along with the $\sigma$ and $\pi$ contributions to the spectra, i.e., density of states. In the low-spin case the $t_{2g}/e_g$ orbital splitting is large relative to electron repulsion, producing a low-energy feature that is pure $\pi$, labeled the "$t_{2g}$ feature".

While there is only one hole in the $t_{2g}$ orbitals in the low-spin configuration, $(t_{2g})^5(e_g)^0$, this feature is well separated from the four transitions to the e holes, and the relative $\pi$ and $\sigma$ contributions to bonding can be quantified. Note from Figure 8, bottom, that for the low-spin complex there is some $\pi$ character mixed into the lower energy side of the $\sigma$ states through CI but that this is included in the VBCI fits.

For Fe(III) high-spin complexes, electron repulsion is large relative to the ligand field splitting, and there is no pure $\pi$ or $\sigma$ feature. However, $\sigma$ and $\pi$ states do distribute differently over the shape of the L-edge spectrum, as indicated by the gray ($\pi$) and black ($\sigma$) states in Figure 8, top. In high-spin $d^5$, the $t_{2g}{}^3e_g{}^2$ configuration gives a 3:2 intensity ratio for the $\pi$:$\sigma$ contributions to the spectrum in the absence of differences in covalency. Thus, the contributions from both the $\pi$- and $\sigma$-orbitals impact the spectral shape. The low-energy spectral feature has more $\pi(t_{2g})$ character than the second, and the spectral shape can still be simulated to extract the DOC.

**4.2. Origin of the Differences in Covalency.** The differences in oxalate, catecholate, and hydroxamate ligand covalent bonding to high-spin Fe(III) described above reflect differences in the natures of the bonding orbitals of the ligands. Before interaction with the metal, there are four sets of mostly O-localized valence orbitals: sym and anti-sym combinations of out-of-plane (op) and in-plane (ip) orbitals, perpendicular to the O−C bonds. The oop form $\pi$ bonds to the Fe, and the ip form $\sigma$ bonds. Each splits into a set of three MOs, as there are three bidentate ligands in the Fe(III) complexes. Contours of these orbitals for oxalate are shown in Figure 9, upper left. Figure 9 shows the $\beta$-spin energy levels for both occupied ligand bonding orbitals and the unoccupied metal d-orbitals; the

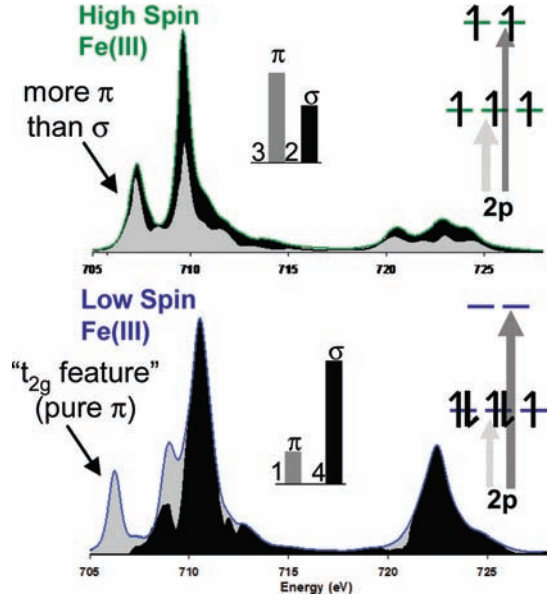


***Figure 8.*** Comparison of the Fe L-edges of a typical high-spin Fe(III) complex (top) and a low-spin Fe(III) complex (bottom). Orbital population insets indicate the origin of $\sigma$ and $\pi$ intensity (arrows) which is then distributed over the states due to e−e repulsion, as indicated by black ($\sigma$) and gray ($\pi$) DOS.

(73) Evers, A.; Hancock, R. D.; Martell, A. E.; Motekaitis, R. J. *Inorg. Chem.* **1989**, *28*, 2189–2195.

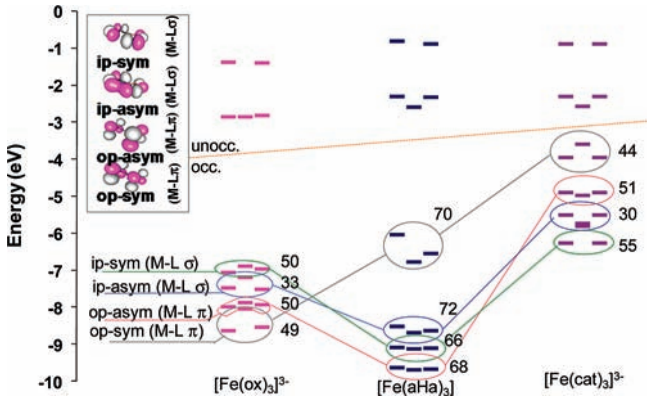


***Figure 9.*** Comparison of the $\beta$ spin energy levels in high-spin Fe(III) tris oxalate, $[Fe(ox)_3]^{3-}$, Fe(III) tris hydroxamate, $[Fe(aha)_3]$, and Fe(III) tris catecholate, $[Fe(cat)_3]^{3-}$. Numbers indicate the O character in the corresponding orbital of the free ligand (shown in the contours, in inset). Lines join the orbitals in the different manifolds with similar intraligand bonding.

numbers offset to the right of the ligand bonding orbitals are the O coefficients as calculated for a free ligand with an ionic counterion ($Na^+$ or $Mg^{2+}$). Each symmetry set of orbitals is circled and correlated with different colored lines to equivalent orbitals on each ligand to facilitate comparison. An equivalent plot of the free ligand orbitals before bonding is given in Supporting Information, Figure S4, which shows similar trends.

In Figure 9, the unoccupied metal orbitals are shown above the line, and occupied ligand donor manifolds are below the line. In the unoccupied d-orbitals in Figure 9, the $D_3$ distortion from $O_h$ symmetry splits the $\pi$ set, particularly in the hydroxamate and catecholate complexes. However, the effect of this $D_3$ distortion on L-edge spectral shape has been evaluated and is given in Supporting Information, Figure S5 (it is minor; *vide supra*).

Importantly, Figure 9 also reveals key differences in the relative energies of the ligand donor orbitals. The entire catecholate bonding manifold (purple, far right) has shifted to higher energy relative to that of oxalate (pink, far left). In addition, the orbital energies have reordered, with the op-sym ($\pi$) orbital (circled in gray, Figure 9) shifting from deepest energy in the oxalate manifold to the highest energy molecular orbital (HOMO) of the catecholate manifold.

When two orbitals interact, the energy gained is approximated by $(H_{M-L})^2/\Delta$, where $\Delta$ is the energy difference between the metal and the ligand orbitals before bonding and $H_{M-L}$ is the resonance integral associated with ligand−metal overlap. As the O coefficients (Figure 9) and Fe−O bond distances (Scheme 1) are similar for oxalate and catecholate, the resonance integrals should be similar for both the $\sigma$ and $\pi$ bonding interactions. Thus, the origin of the increased $\sigma$ and $\pi$ donation in $[Fe(cat)_3]^{3-}$ relative to $[Fe(ox)_3]^{3-}$ is the decreased orbital energy difference $\Delta$. This is reflected in the absorption spectra by the presence of the low-energy intense $\pi$ charge-transfer band in $[Fe(cat)_3]^{3-}$,[10] which is absent in $[Fe(ox)_3]^{3-}$.[74] This energy difference reflects the bonding differences of the two ligand fragments; the O−C distance directly adjoining the Fe−O bond is substantially shorter in oxalate, 1.28 Å, compared to catecholate, 1.34 Å (Scheme 1). The shorter bond length in ox indicates the system is more $\pi$ delocalized over the $O_2C$ fragment and therefore stabilized in energy, decreasing its $\pi$ interaction with the $Fe^{III}$.[75,76]

For the hydroxamate, it is more difficult to estimate the relative contributions because the O character in the valence orbitals is quite different. While the covalent contribution to bonding is higher than for the ox (Table 4), the strength of the Fe(III)−hydroxamate bond is substantially weaker due to the lower ionic contribution to bonding (Table 5). In solvent this weaker bond is more than compensated by the reduced solvation of the hydroxamate relative to the dianionic catecholate and oxalate.

**4.3. Stability Constants.** The spectral shapes of the Fe L-edges in Figure 3 have been analyzed and used to quantify the differential orbital covalencies of the catecholate and hydroxamate complexes relative to oxalate. The results in Table 4 quantify the electronic structure contributions to the high stability constants in terms of $\sigma$ and $\pi$ covalent contributions to bonding from experimental covalencies. As the coefficients of O character in ox and cat orbitals are similar (Figure 9), we can estimate the relative energy contributions to bonding from the experimental $\sigma$ and $\pi$ covalencies. From the above discussion, the bonding energy is proportional to $(H_{M-L})^2/\Delta$, while the coefficient squared of ligand character in the metal d-orbital (i.e., covalency) is proportional to $(H_{M-L}/\Delta)^2$. Therefore, the bonding energy is proportional to the covalency scaled by the energy differences of the interacting orbitals (energy $\propto$ (coefficient)$^2\Delta$). On the basis of a combination of the VBCI fits (Table 4) and DFT calculations (Figure 9), we can estimate $\Delta$ and the coefficients of mixing for ox and cat complexes.[77] This analysis indicates that ~20% of the energy difference between $[Fe(ox)_3]^{3-}$ and $[Fe(cat)_3]^{3-}$ is due to the increase in $\pi$ bonding; the larger contribution is in fact due to the increase in $\sigma$ bonding, even though the $\sigma$- and $\pi$-orbital covalencies increase by similar amounts (20% $\Delta\pi$, 17% $\Delta\sigma$, Table 4). The larger contribution to the increase in bond strength from a similar increase in $\sigma$ relative to $\pi$ covalency reflects the larger energy separation of the ligand $\sigma$ donor orbitals from the metal levels, Figure 9. Thus a more limited contribution to the covalency from deeper energy orbitals can still make a significant energy contribution to bond strength.

**Acknowledgment.** R.K.H. thanks Dr. Erik C. Wasinger and Dr. Ritimukta Sarangi for their assistance with the multiplet program and beam line operations at SSRL. We would like to acknowledge early contributions to this work by Dr. Tami Westre, Ms. Ekaterina Y. Shishova, and Drs. Emily Dertz and Jide Xu. This work was supported by grants from the NIH GM-40392 and NSF CHE-0446304 to E.I.S., NIH RR-01209 to K.O.H, and NIH AI11744 to K.N.R. The synchrotron data described herein were collected at SSRL, which is funded by the U.S. DOE Office of Basic Energy Sciences. The SSRL Structural Molecular Biology Program is supported by the NIH National Center for Research Resources, Biomedical Technology Program, and by the U.S. DOE Office of Biological and Environmental

(74) Holt, S.; Dingle, R. *Acta Chem. Scand.* **1968**, *22*, 1091–1095.

(75) Pau, M. Y. M.; Davis, M. I.; Orville, A. M.; Lipscomb, J. D.; Solomon, E. I. *J. Am. Chem. Soc.* **2007**, *129*, 1944–1958.

(76) Pau, M. Y. M.; Lipscomb, J. D.; Solomon, E. I. *Proc. Natl. Acad. Sci. U.S.A.* **2007**, *104*, 18355–18362.

(77) For $[Fe(cat)_3]^{3-}$: d$\pi$ $\Delta$ = 2.0 eV and 26% ligand character, therefore $E \propto (0.26)(2.0) = 0.52$; d$\sigma$ $\Delta$ = 5.5 eV and 48% ligand character, therefore $E \propto (0.48)(5.5) = 2.64$ eV. For $[Fe(ox)_3]^{3-}$: d$\pi$ $\Delta$ = 6.0 eV and 6% ligand character, therefore $E \propto (0.06)(6) = 0.36$ eV; d$\sigma$ $\Delta$ = 6.0 eV, 31% ligand character, therefore $E \propto (0.31)(6) = 1.86$ eV. The total energy difference $[Fe(cat)_3]^{3-}-[Fe(ox)_3]^{3-} = 0.94$ eV; total energy difference d$\pi$ = 0.16 eV or 17% of total energy.

Research. The NCI national facility in Australia and the Monash Sun Grid are acknowledged for access to computer time.

**Supporting Information Available:** Complete refs 36 and 37; Table S1, energies and intensities of the fits to the Fe K pre-edges shown in Figure 2; Figure S1, effect of d−d spin orbit on the spectrum of high-spin Fe(III); Figure S2, set of simulations used to generate Figure 6, along with a more detailed explanation of the derivation of Figure 6; Figure S3, expansion of the energy region to show both $L_3$ and $L_2$ shown in Figure 7; Figure S4, four highest occupied orbitals of the free ligands prior to bonding; Table S2, key geometric parameters from the geometry optimization; Table S3, comparison of calculated and experimental thermodynamics values for tris Fe, Ga, and Al complexes of oxalate, hydroxamate, and catecholate; Figure S5, octahedral and lower symmetry multiplet simulations. This material is available free of charge via the Internet at http://pubs.acs.org.

JA9090098